Supplementary Information

Elevated CO_2 increases leaf temperature independently of stomatal regulation

David Helman[1,2,*], Gabriel Mulero[1,2] and Emmanuel Tamata[1]

1. Department of Soil & Water Sciences, Institute of Environmental Sciences, The Robert H. Smith Faculty of Agriculture, Food and Environment, The Hebrew University of Jerusalem, Rehovot 7610001, Israel.
2. The Advanced School for Environmental Studies, The Hebrew University of Jerusalem, Givat Ram, Jerusalem 9190401, Israel.

[*]Corresponding author: david.helman@mail.huji.ac.il

The FACE system and its experimental design

The study was conducted at the WheatDryFACE facility (Figure S1), operating since August 2022 at the Hebrew University of Jerusalem's experimental farm in Rehovot, Israel (34°47`N, 31°54`E: 54 m a.s.l). The area is characterized by a Mediterranean climate with a long-term (14 years; 2006–2020) mean daily temperature of 21.1°C ± 5.4°C, and a mean total annual precipitation of 540 ± 55 mm y^{-1} [1]. The facility comprises six plots arranged in a randomized complete block split-plot design, including three free-air CO_2 enrichment (FACE) rings enriched to a target [CO_2] level of *c.* 600 µmol mol^{-1}, and three control plots maintained at ambient [CO_2] levels (Figure S2). Ring placement accounted for the predominant wind direction to minimize CO_2 cross-contamination between treatments.

Each enrichment ring is designed as an octagonal ring, 8 m in diameter and enclosing an area of approximately 50 m^2 (Figure S3), constructed by engineers from Azrieli College of Engineering, Jerusalem. The rings consisted of eight iron masts arranged as an octagon, each supporting a PVC pipe connected to the main CO_2 supply line. CO_2 was released through 4-mm perforations in the PVC pipes positioned around the ring perimeter. Gas flow to each ring was regulated by a pressure gauge based on its distance from the main CO_2 storage tank, and a datalogger-based control unit positioned adjacent to each ring controlled the solenoid on/off valves for automated gas release. The control system operated based on the [CO_2] measured at the center of each ring, along with wind speed and wind direction, such that only the relevant upwind sides of the octagon released CO_2, generally following the FACE principles described by refs-[2,3]. The control unit was scheduled to operate during daytime hours, opening valves from 06:30 to 17:00. During this operating period, valves opened to 70% of capacity when 10-min mean wind speed was ≤ 1 m s^{-1} and ring-center [CO_2] was below 550 µmol mol^{-1}, whereas gas release was halted when wind speed reached ≥ 8 m s^{-1} and/or [CO_2] exceeded target concentration. Actual measured [CO_2] in the plots were 581±66 µmol mol^{-1} for elevated and 421±21 µmol mol^{-1} for ambient CO_2 plots.

[CO_2] in each enrichment ring were monitored continuously using a factory-calibrated infrared gas analyzer (WMA-5, PP systems Ltd, Amesbury, MA, USA) installed at the ring center (Figure S3). To further characterize the spatial distribution of [CO_2] within enrichment rings, a lab-built low-cost monitoring system was deployed (Figure S4a,b). This system consisted of SCD30 [CO_2] sensors (Sensirion AG, Stäfa, Switzerland) coupled to WeMos ESP32 D1 mini boards programmed to record data every 5 min. Twelve sensors were installed equidistantly within two enrichment rings at 1 m above ground level, although data from only one ring are reported here due to technical issues in the second ring. Sensor data were streamed to the ThingSpeak online platform and calibrated in situ against the central WMA-5 analyzer before the beginning of enrichment in the

first year of the WheatDryFACE project. After linear calibration, no significant differences were detected between the calibrated low-cost sensors and the reference analyzer during the pre-enrichment calibration period (Dunnett's test, $p < 0.05$; Figure S4c,d). Monthly and seasonal averages during enrichment periods were subsequently used to map within-ring [CO_2] distribution and evaluate its relationship with wind conditions (Figure S5).

Installed within the WheatDryFACE field was a sensor network for microclimate monitoring (Figures S2 and S3). Air temperature and relative humidity (*RH*; %) were measured using a Vaisala HMP-series HUMICAP® probe (Vaisala Oyj, Vantaa, Finland). Wind speed and wind direction were measured at 2 m above ground with a Wind Sentry anemometer (Model 03002; R.M. Young Company, Traverse City, MI, USA). Precipitation was recorded using a tipping-bucket rain gauge (Model 52203; R.M. Young Company, Traverse City, MI, USA). Incoming shortwave and longwave radiation were measured at 2.5 m height using a thermopile pyranometer (SP-510-SS) and pyrgeometer (SL-510-SS; Apogee Instruments, Logan, UT, USA), respectively. All meteorological data were logged automatically at 5-min intervals. Photosynthetically active radiation (*PAR*; μmol m^{-2} s^{-1}) was estimated from incoming shortwave radiation using a quantum-to-energy conversion factor (2.02 μmol J^{-1}) [4]. Within each ring, soil volumetric water content (*VWC*; %) and soil temperature (T_{soil}; °C) were measured at 20 and 55 cm depth using TDR-315H time-domain reflectometry sensors (Acclima Inc., Meridian, ID, USA); however, only data from 20 cm depth were used in the present study.

Water regimes were managed using a retractable rain-exclusion system consisting of an 8 × 4 m frame fitted with corrugated polycarbonate sheeting (SUNTUF, Palram Ltd., Ramat Yohanan, Israel), which covered half of the plot/ring area during exclusion events and remained retracted under normal conditions (Figure S6). Accordingly, the water treatment was applied as a split-plot factor within each ring. The shelters were deployed during rain events to facilitate two water regimes: well-watered (WW) and water-limited (WL).

In *Season 1* (2023/24), the total amount of rain and irrigation was 512 mm for the entire season (from two weeks before sowing – 12 November 2023 – to harvest – 19 March 2024) and 464 mm during the measurement period (up to the last thermal imaging on 22 February 2024). WL plots in that season received 323 mm, a reduction of 141 mm over the measurement period. In *Season 2* (2024/25), total water from rain and irrigation was less than in the first season – 434 mm for the entire season (from two weeks before sowing – 18 November 2024 – to harvest – 26 April 2025) and 403 mm during the measurement period (up to the last thermal imaging on 26 March 2025), with only 31 mm of rainwater excluded in the WL plots over the measurement period (a total of 372 mm).

Two Israeli wheat genotypes, cv. *Zahir* (early-maturing) and cv. *Ruta* (late-maturing) [5,6] were cultivated (Figures S7 and S8). Each genotype was sown in sub-plots across all [CO_2] and water treatments.

Although the WheatDryFACE has been operating for the last three years, we used data from only the last two years in this study, since thermal images were taken only in these two years. Detailed meteorological conditions for both seasons are summarized in Table S1.

Relationships with ΔT and statistically-derived [CO_2]-driven mechanisms

Before modeling ΔT, we examined its relationships with various variables (Figure S18). While ΔT had parallel linear relationships with g_{sw}, T_r, *VWC*, and *PAR* at ambient and elevated [CO_2] conditions, it had contrasting ambient-to-elevated [CO_2] relationships with the other variables, likely indicating confounding processes under elevated [CO_2]. The full parametric and non-parametric relationships among the time-variant variables are presented in Figure S19 and Figure S20, respectively.

To further evaluate the complex mechanisms by which elevated [CO_2] influences ΔT, we implemented a sequential model-building framework in which candidate variables representing different biophysical processes were added stepwise to a baseline model. To account for potential non-linear relationships, we used an ordinary least squares (OLS) model of a quadratic form. OLS was used because it provides an interpretable framework for estimating the contribution of multiple predictors to variation in ΔT and for quantifying how the estimated CO_2 effect changes when additional explanatory variables are introduced. In this framework, model coefficients are estimated by minimizing the sum of squared differences between observed and predicted ΔT. The model remains linear in its coefficients, while the inclusion of quadratic terms allows for non-linear relationships between the predictors and ΔT.

The baseline model (B) includes CO_2 as the primary explanatory variable, together with background environmental control variables so that the explanatory contribution of the candidate mechanistic variables (g_{sw}, *LAI*, height, and T_{soil}) could be evaluated in subsequent model expansions. Genotype (G), water (W) and DAS were all included in B as categorical factors. Thus, B reads as follows:

$$\Delta T\,(^{\circ}\mathrm{C}) = \beta_0 + \beta_{CO_2}[CO_2] + \sum(\beta_i X_i + \gamma_i X_i^2) + \mathrm{G} + \mathrm{W} + \mathrm{DAS} + \epsilon_i \qquad (2)$$

where β_{CO_2} in (2) represents the effect of CO_2 on ΔT, and X_i represents the control variables *VPD*, *SWC*, *PAR*, and wind speed. These variables were calculated as daily means within the active measurement window for each sampling date.

We then expanded the baseline model stepwise by introducing variables corresponding to specific hypothesized mechanisms. First, g_{sw} was added to represent physiological control of evaporative cooling (B + g_{sw}). Next, canopy structural variables (*LAI* and canopy height) were introduced to account for the effects of canopy development on radiative loading and aerodynamic coupling (B + g_{sw} + *LAI* and B + g_{sw} + *LAI* + height). Finally, T_{soil} was included as a proxy for soil-related thermal and radiative conditions (full model). Because complete replicate coverage across all dates was only available in *Season 2*, the sequential attribution analysis was performed using *Season 2* data only. All analyses were conducted on plot-level means for each sampling date (N = 144).

At each step, the model was re-fitted and the shift in β_{CO_2} was re-estimated:

$$\beta_{CO_2}\text{shift (\%)} = \left(\frac{\beta^{\,i}_{CO_2} - \beta^{\,baseline}_{CO_2}}{\beta^{\,baseline}_{CO_2}}\right) \times 100 \quad (3)$$

where $\beta^{\,baseline}_{CO_2}$ and $\beta^{\,i}_{CO_2}$ are the [CO_2] coefficients in the baseline (B) and expanded model (B + g_{sw}, B + g_{sw} + *LAI*, B + g_{sw} + *LAI* + height, and full model), respectively.

β_{CO_2} shift was then used to quantify the extent to which the newly introduced variables accounted for the observed CO_2 effect on ΔT. In this framework, a reduction in β_{CO_2} indicates that the added variable explains part of the CO_2-associated variation in ΔT, whereas a negligible change indicates limited explanatory power. Because each expanded model is nested within the previous one, this sequential approach allows for a structured evaluation of competing mechanisms and their relative contribution to the observed warming. The interpretation is therefore one of explanatory attribution within the nested modelling framework. Multiple model specifications were evaluated (Table S3), but only those representing the primary hypothesized mechanisms are presented in the main text (Table S4).

To further interpret the selected model (Table S4), we examined partial-effect response curves for specific predictors. These were used to visualize how changes in the selected variables were associated with modeled changes in ΔT, while the remaining terms in the model were held constant.

Supplementary Figures

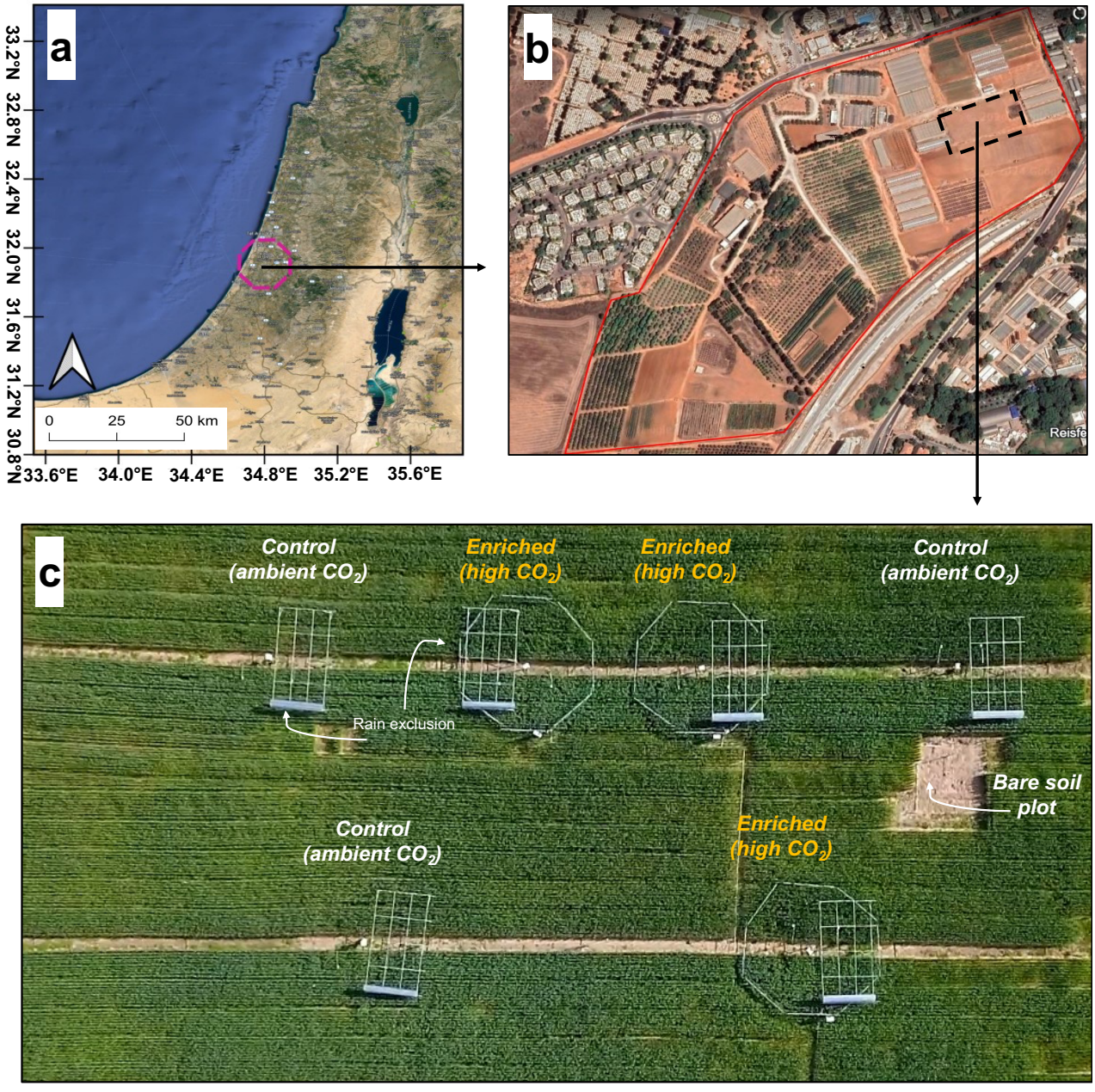

Figure S1. (a) Location of the study area in Israel, Rehovot. (b) An overview of the experimental field within the Robert H. Smith, Faculty of Agriculture's Research Farm (red polygon). (c) UAV RGB orthomosaic of the WheatDryFACE experimental field with all six experimental treatment rings.

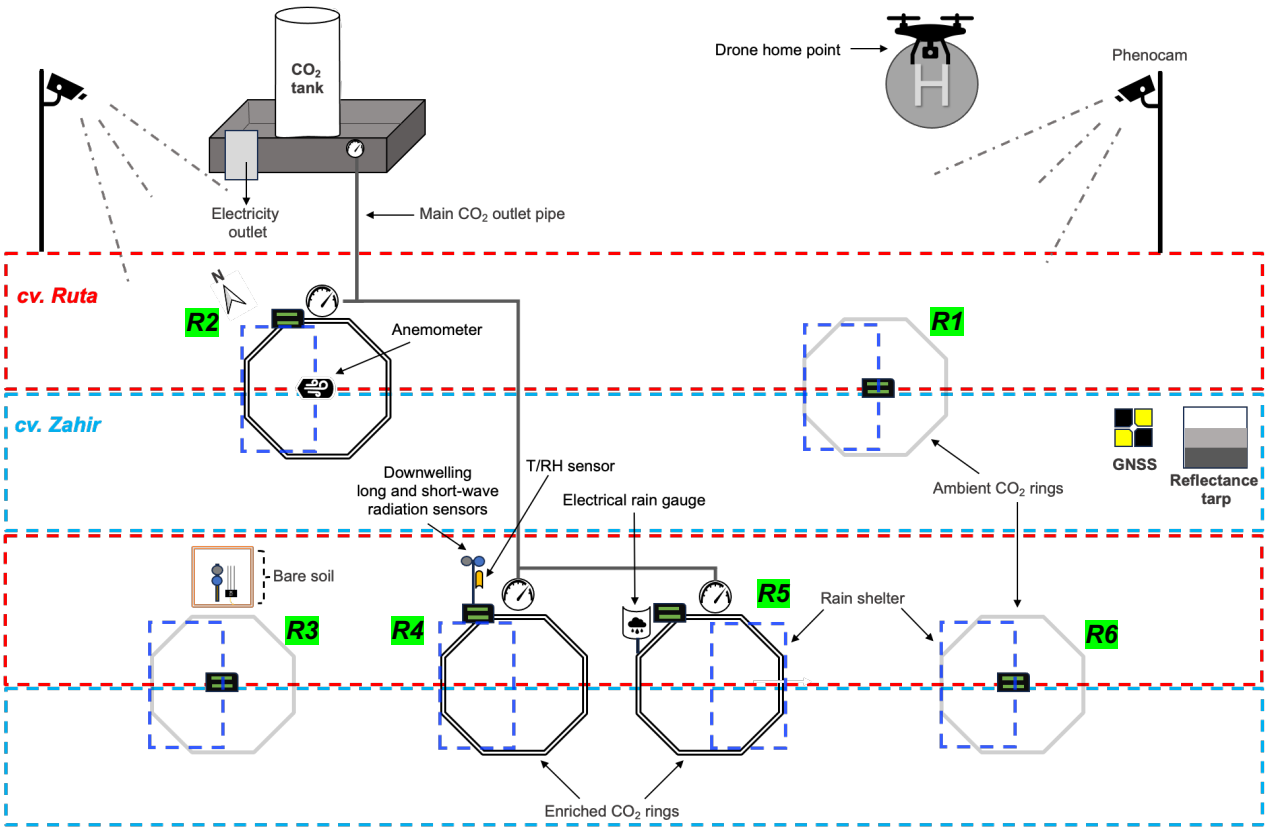

140

141 Figure S2. Schematic of the WheatDryFACE experimental field. The [CO_2] enriched rings (*R2*, *R4*
142 and *R5*) are 8 m in diameter. The wheat genotypes (cv. *Zahir* and *Ruta*) are set up in alternating
143 areas. Bare soil with sensors is set up as a control plot for both soil water content and outgoing
144 radiation data. Within the project, an unmanned aerial vehicle (UAV) is flown; thus, we often set
145 up a 3 by 3 m reflectance tarp in the field and a high-precision GNSS receiver – Trimble SPS585.
146 Two PhenoCam cameras are installed at a height of 4 m facing the field (see images in Fig. S6) to
147 monitor crop growth during the growing season.

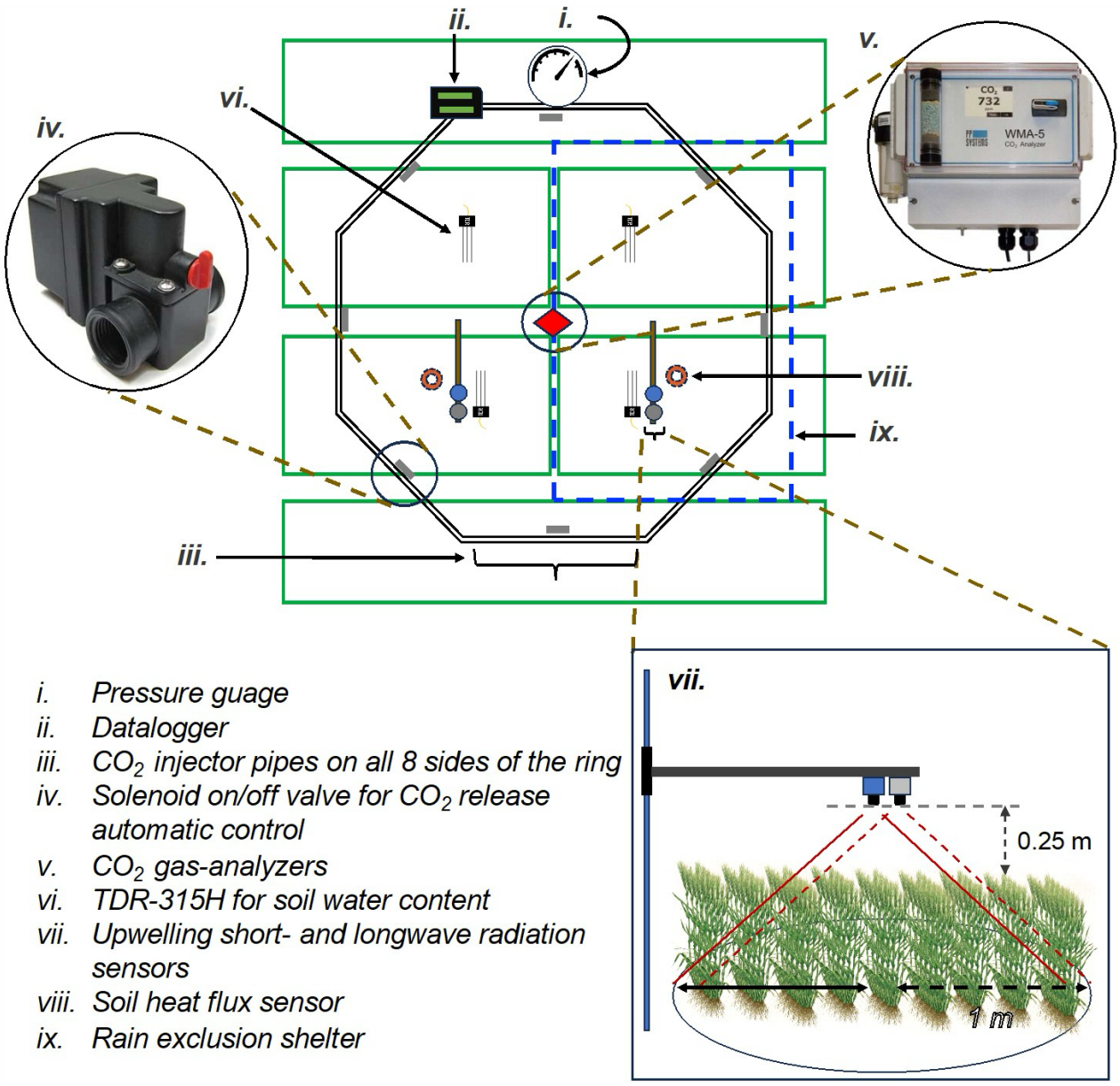

i. Pressure guage
ii. Datalogger
iii. CO_2 injector pipes on all 8 sides of the ring
iv. Solenoid on/off valve for CO_2 release automatic control
v. CO_2 gas-analyzers
vi. TDR-315H for soil water content
vii. Upwelling short- and longwave radiation sensors
viii. Soil heat flux sensor
ix. Rain exclusion shelter

Figure S3. Schematics of a typical octagonal ring with [CO_2] enrichment in WheatDryFACE, showing major sensors installed within the enriched ring area. All items, except *iii* and *iv,* were installed in the ambient [CO_2] plots as well.

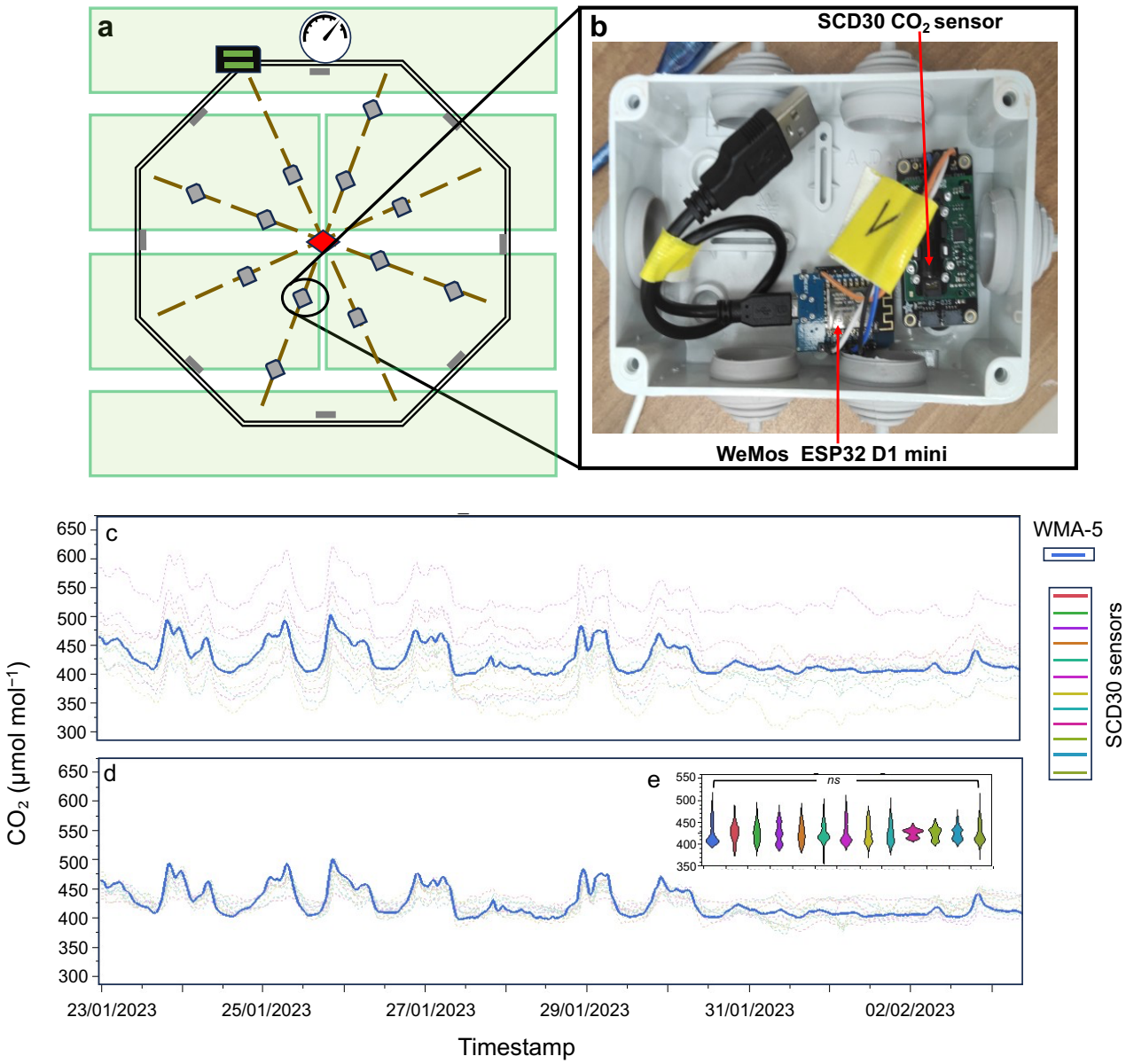

152

153 Figure S4 (a) Schematics of a [CO_2]-enriched octagonal ring showing the spatial distribution of (b)
154 low-cost [CO_2] sensors built at our lab and placed at the top of the canopy, 1 m above the ground,
155 across the ring area. (c) [CO_2] readings from the SCD30 sensors before onsite-calibration with the
156 high-end WMA-5 PP system CO_2 analyzer. (d) [CO_2] readings after on-site calibration with the
157 WMA-5 PP system CO_2 analyzer using a linear calibration function for each sensor. (e) Insert
158 showing Dunnett's test between all calibrated SCD30 sensors against the WMA-5 PP system CO_2
159 analyzer reading, showing no significant differences at $p < 0.05$ between the sensors after
160 calibration for the entire period before enrichment.

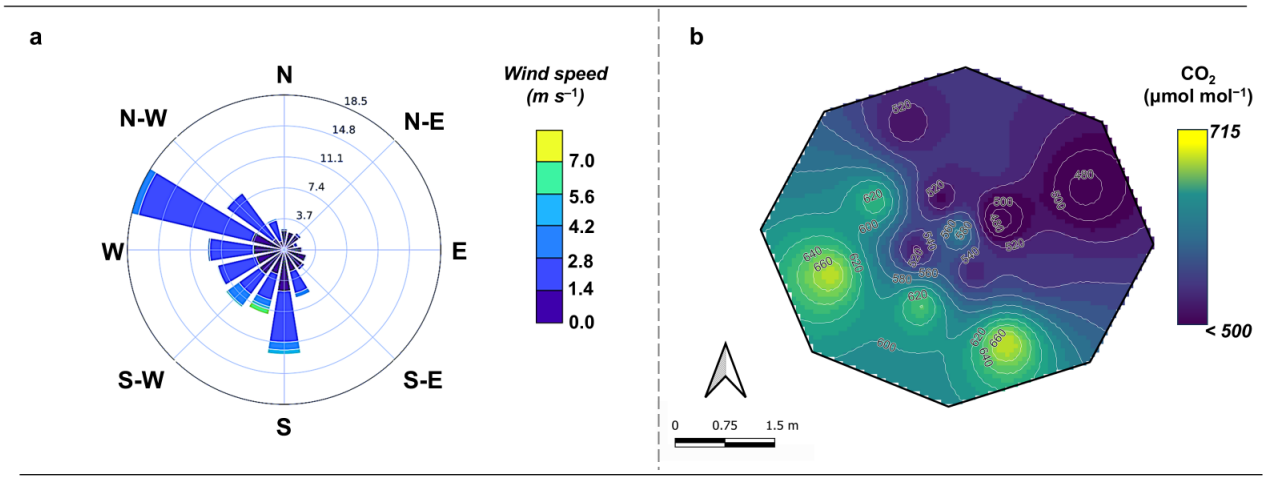

161

162 Figure S5. (a) Windrose representation of the mean wind speed (m s^{-1}) and directions (°) and (b)
163 interpolated spatial distribution of the mean [CO_2] within a single [CO_2]-enriched octagonal ring
164 for the active enrichment period.

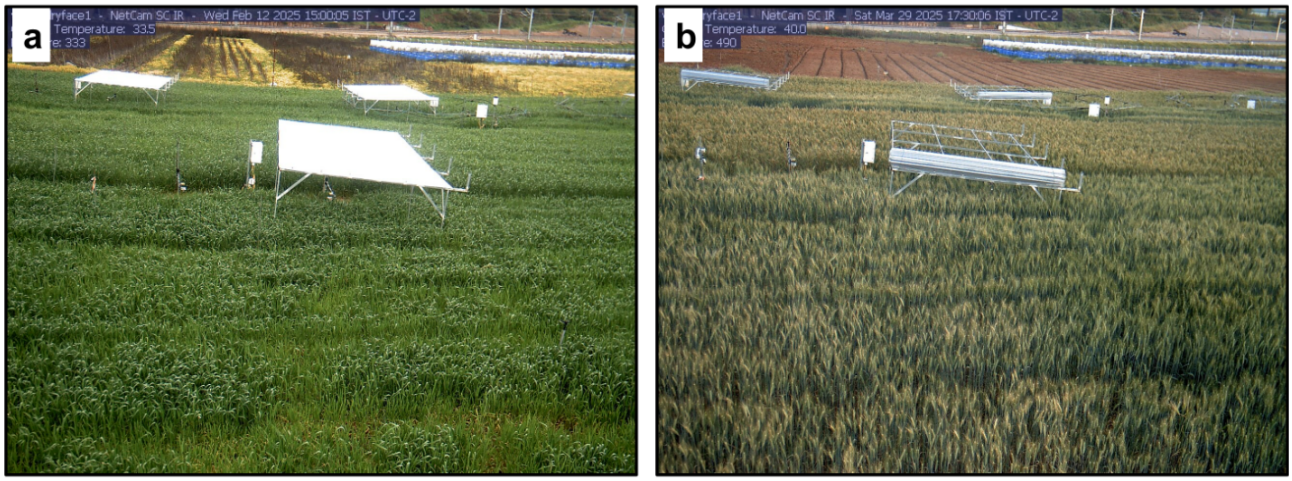

165

166 Figure S6. Retractable rain-exclusion system used at the WheatDryFACE facility. (a) PhenoCam
167 image showing a rain-exclusion shelter deployed above the wheat canopy during a rainfall event.
168 (b) The same shelter in its retracted position under non-rain conditions. Both images were captured
169 by the field-installed PhenoCam cameras.

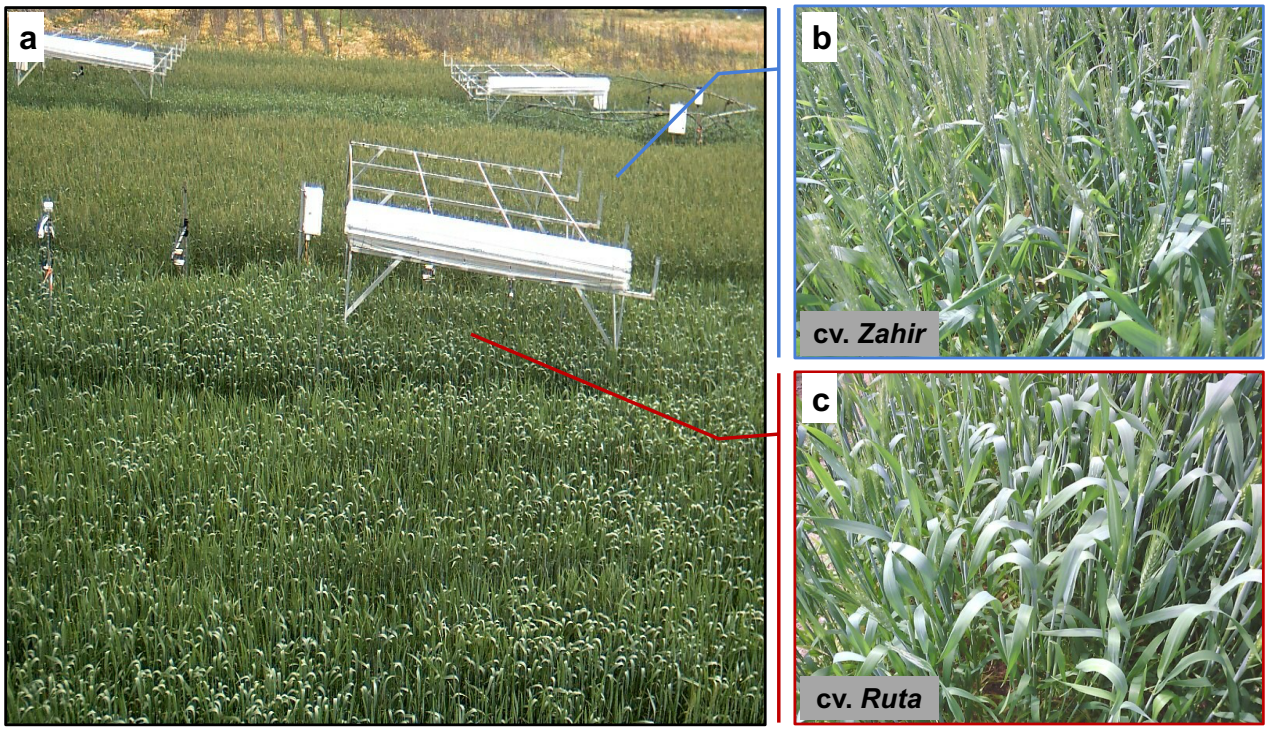

Figure S7. Representative field images of the two wheat genotypes used in the experiment. (a) Field view showing adjacent plots of the two cultivars. Close-up pictures of (b) cv. *Zahir* at DC65 (anthesis) and (c) cv. *Ruta* at DC52 (heading). Images were acquired on the same day (4 March 2025) and illustrate the contrasting phenological development of the two cultivars.

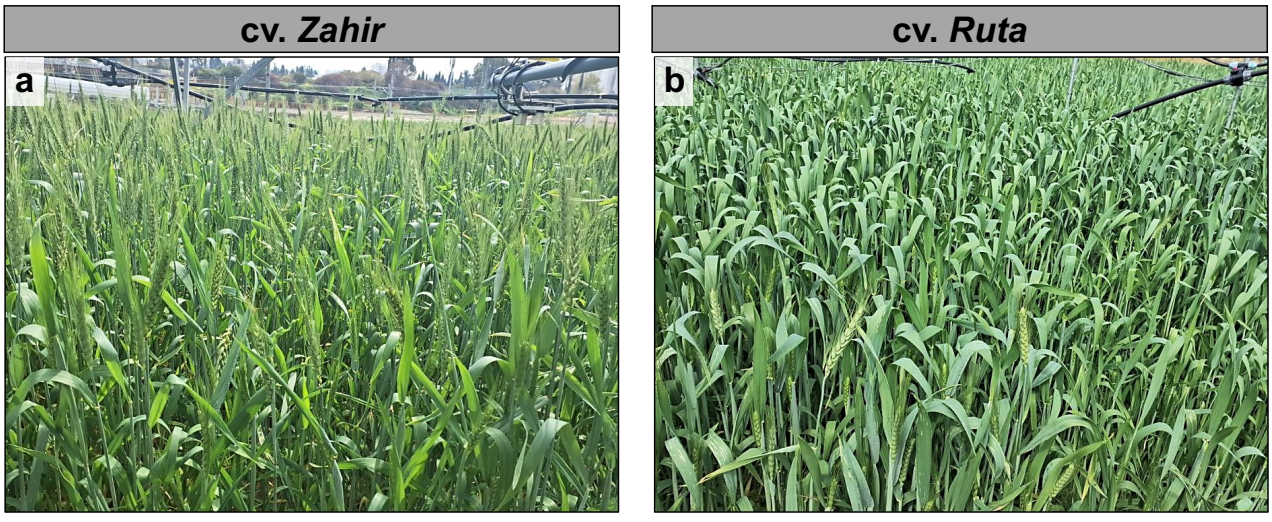

Figure S8. A closer look at the color and structural differences among the two genotypes (a) cv. *Zahir* and (b) cv. *Ruta*. Images were taken on the same day (4 March 2025).

Figure S9. Field preparation, installation, and operation of the WheatDryFACE facility. (a–h) Representative photographs of team members establishing and operating the facility. Panels show (a) TDR sensor installation and system setup, (b) trenching and underground infrastructure preparation, (c) installation of the PhenoCam cameras (Mr. Gil Lerner – lab technician), (d) field sowing with mechanical planter, (e) assembly and adjustment of FACE ring, (f) rain exclusion shelter installation during the growing season, and in-season (g) *LAI* data collection and (h) thermal imaging taken by Emannuel Tamata (MSc).

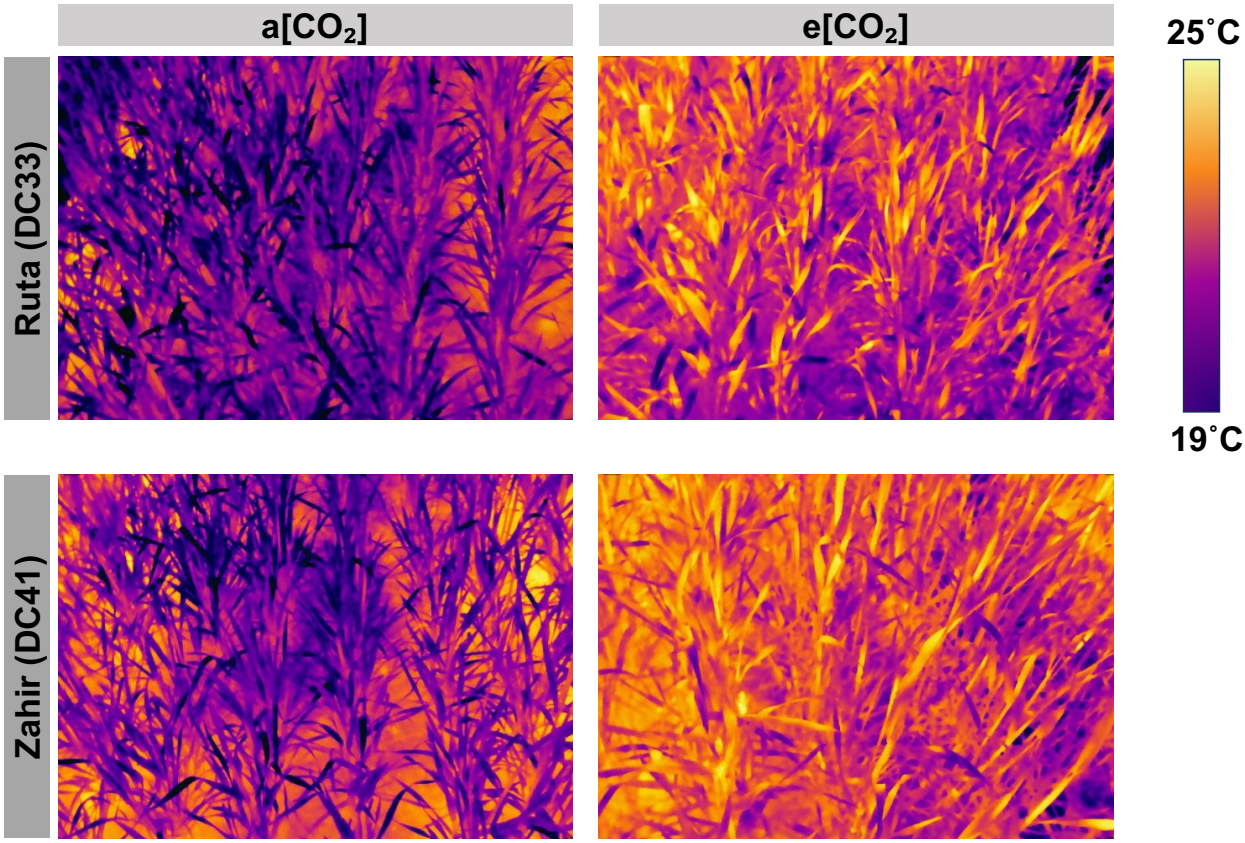

187

188 Figure S10. Thermal images from the FLIR T560 of cv. *Ruta* (DC33) and cv. *Zahir* (DC41) plants
189 taken on the same date and hour (22 January 2024, corresponding to DAS 57) in ambient (aCO_2)
190 and [CO_2]-enriched plots, showing substantially warmer leaves under elevated [CO_2]. Colors
191 indicate the canopy's surface temperature. All values are given in °C.

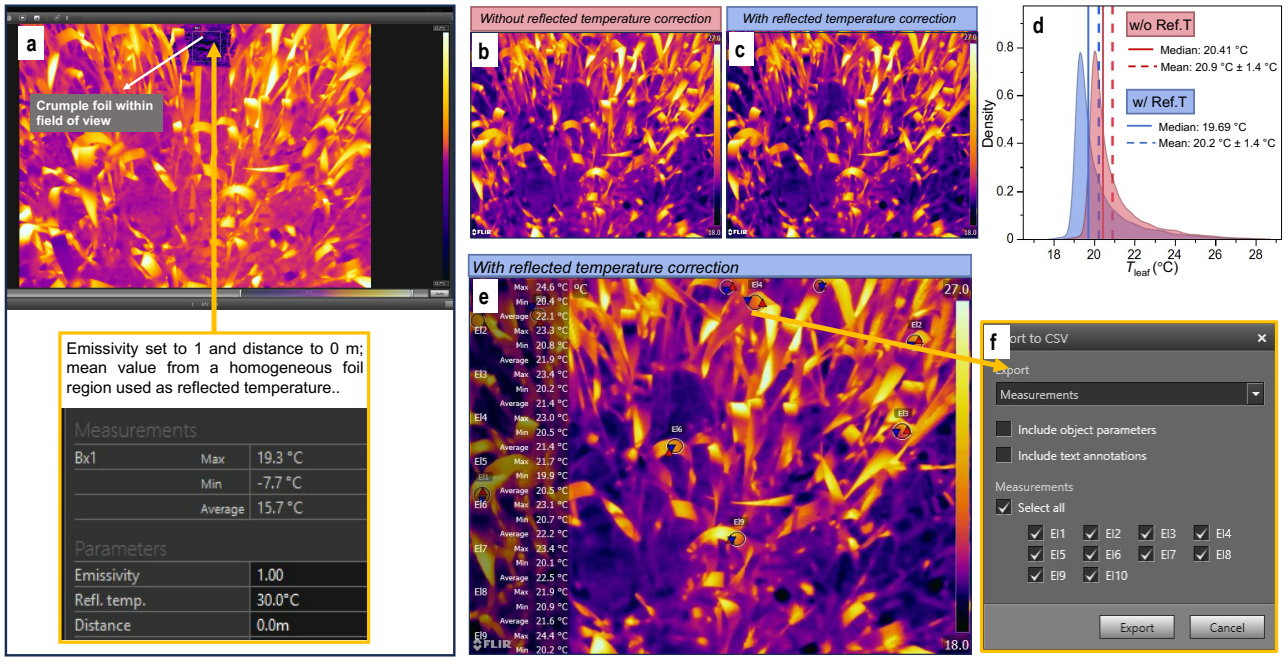

Figure S11. Thermal image processing workflow, including correction of reflected apparent temperature using the crumpled aluminum foil method. (a) Thermal image showing placement of crumpled aluminum foil within the field of view. Emissivity was set to 1 and distance to 0 m, and the mean temperature of a homogeneous foil region was used as reflected apparent temperature. (b) Thermal image processed without reflected temperature correction. (c, e) Thermal images processed with reflected temperature correction applied. (d) Distribution of leaf temperature (T_{leaf}) values extracted from the whole images with (blue) and without (red) reflected temperature correction. Vertical lines indicate median (solid) and mean (dashed; ± SD) values. (e) Extraction of sunlit region-of-interest using ellipse polygon across 10 flag-leaf from the corrected thermal image. (f) final export of T_{leaf} as csv for onward data analysis.

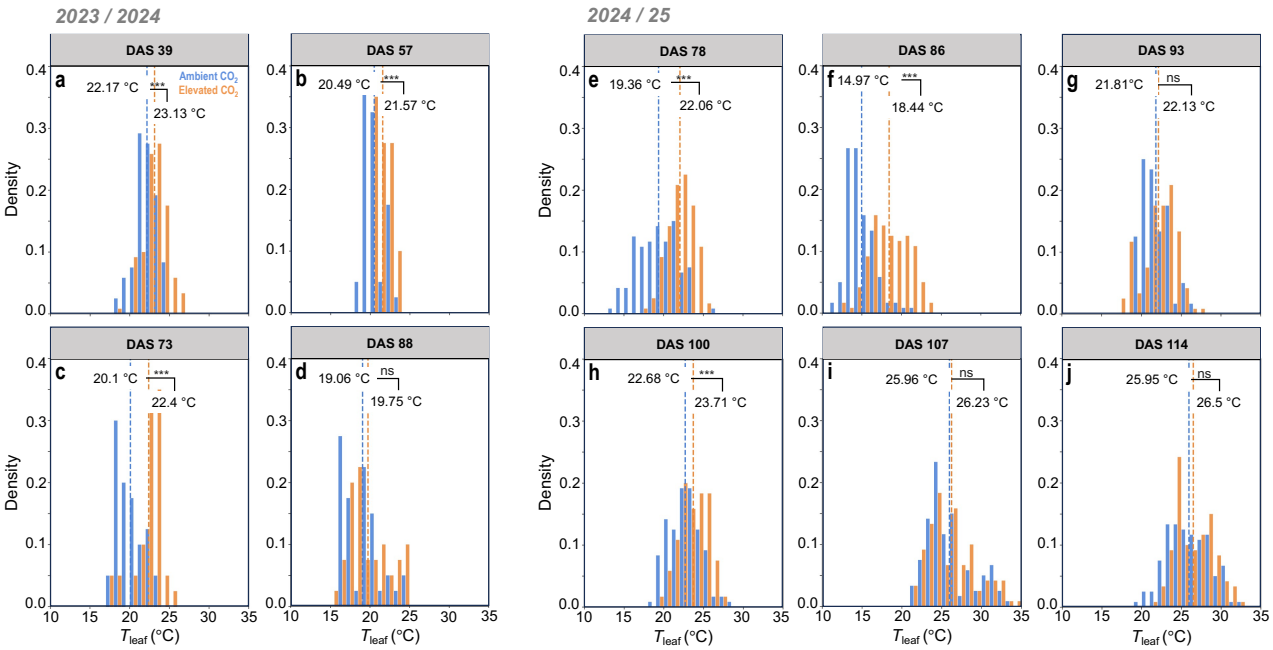

203

204 Figure S12. Density distributions of leaf temperature (T_{leaf}) under ambient (blue) and elevated
205 (orange) [CO_2] for (a–d) *Season 1* (2023/24) and (e–j) *Season 2* (2024/25) across developmental
206 stages (days after sowing, DAS). Vertical dashed lines indicate treatment means. Elevated [CO_2]
207 generally resulted in higher canopy temperatures, with variability across developmental stages.
208 Asterisks denote significant differences between CO_2 treatments (two-tailed *t*-test: *** $p < 0.001$),
209 while non-significant differences are indicated as "ns".

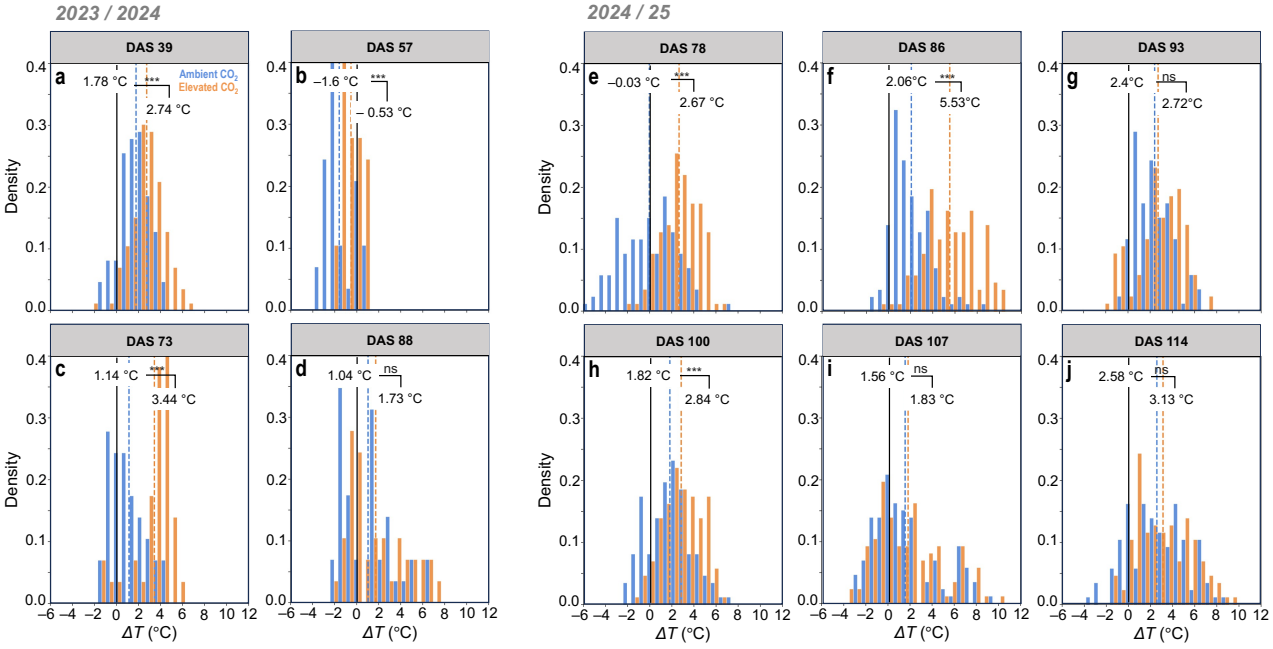

210

211 Figure S13. Same as Fig. S12 but for ΔT.

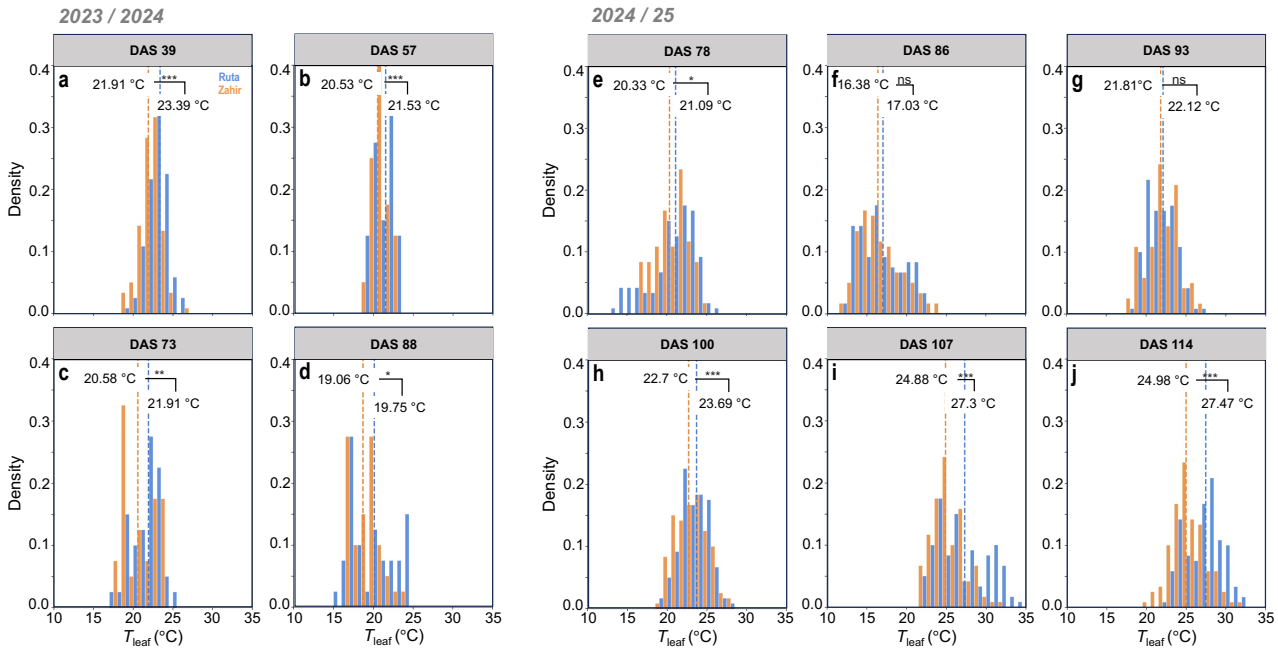

Figure S14. Density distributions of leaf temperature (T_{leaf}) for the two genotypes, cv. *Ruta* (blue) and cv. *Zahir* (orange), across developmental stages (days after sowing, DAS) for (a–d) *Season 1* (2023/24) and (e–j) *Season 2* (2024/25). Vertical dashed lines indicate the means. Differences between genotypes varied across developmental stages, with cv. *Ruta* generally exhibiting higher T_{leaf} than cv. *Zahir* at later stages. Asterisks denote significant differences between genotypes (two-tailed *t*-test: $^{***}p < 0.001$, $^{**}p < 0.01$, and $^{*}p < 0.05$), while non-significant differences are indicated as "ns".

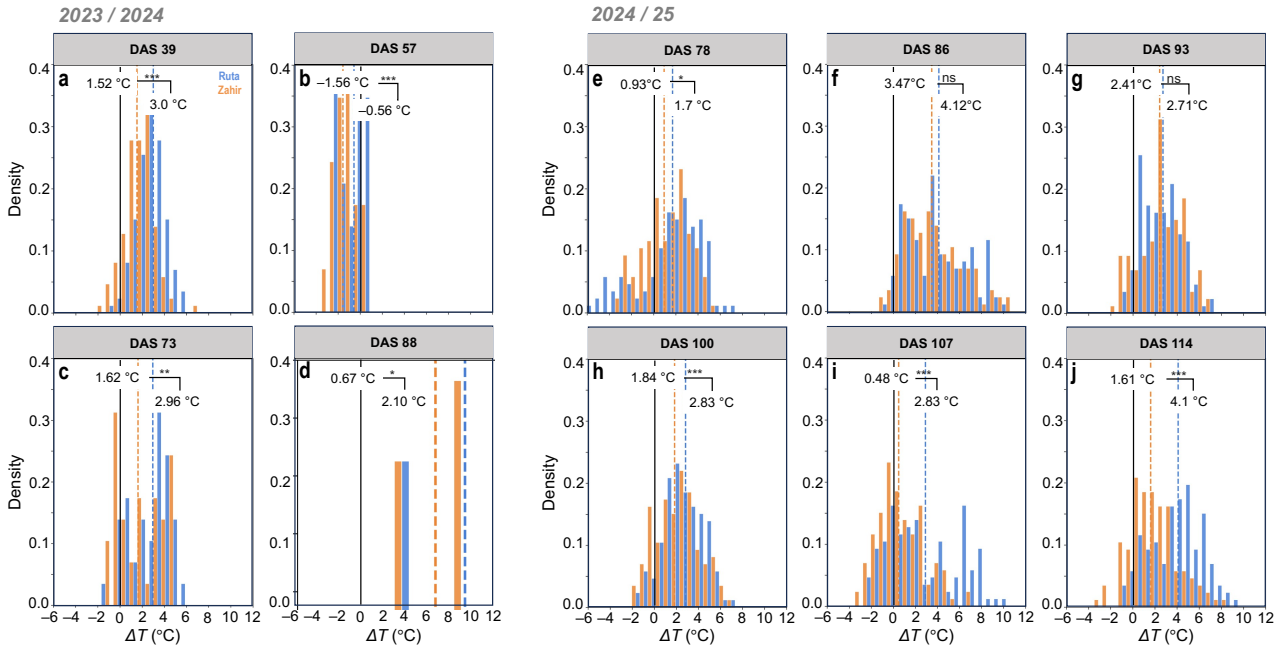

Figure S15. Same ad Figure S14 but for ΔT.

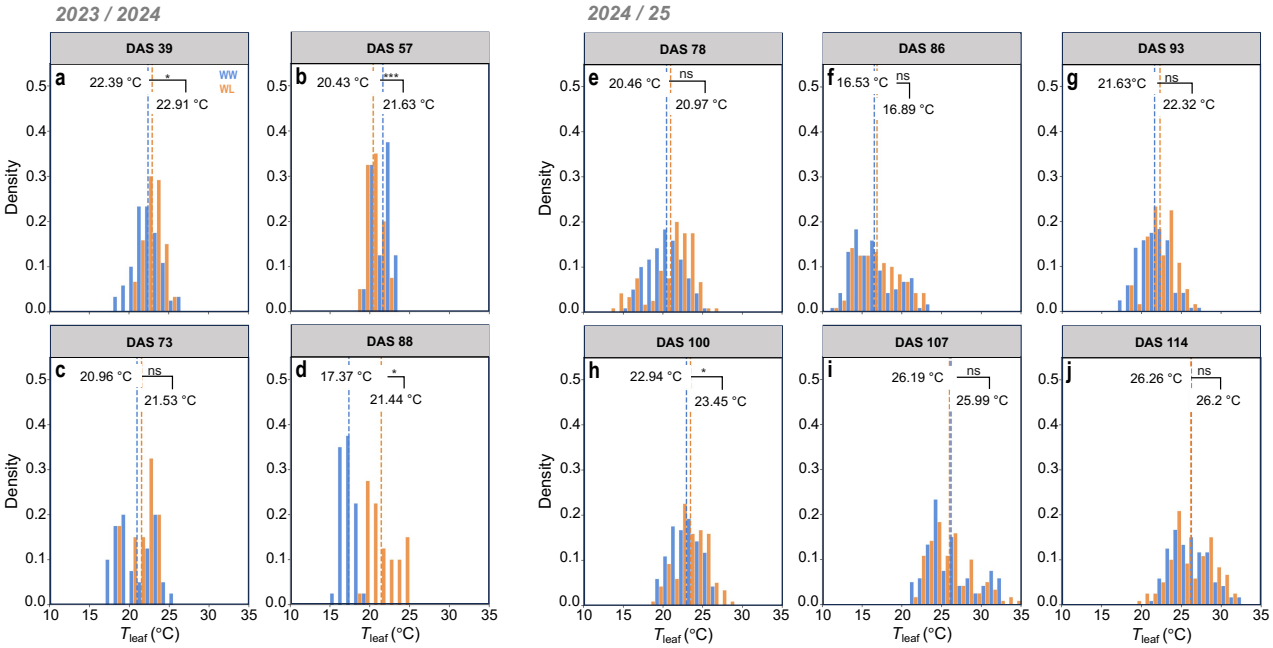

Figure S16. Density distributions of leaf temperature (T_{leaf}) under well-watered (WW, blue) and water-limited (WL, orange) conditions across developmental stages (days after sowing, DAS) for (a–d) *Season 1* (2023/24) and (e–j) *Season 2* (2024/25). Vertical dashed lines indicate treatment means. Differences between water treatments varied across developmental stages, with variability in both magnitude and direction, with generally higher T_{leaf} under water-limited conditions. Asterisks denote significant differences between water treatments (two-tailed *t*-test: *** $p < 0.001$, ** $p < 0.01$, and * $p < 0.05$), while non-significant differences are indicated as "ns".

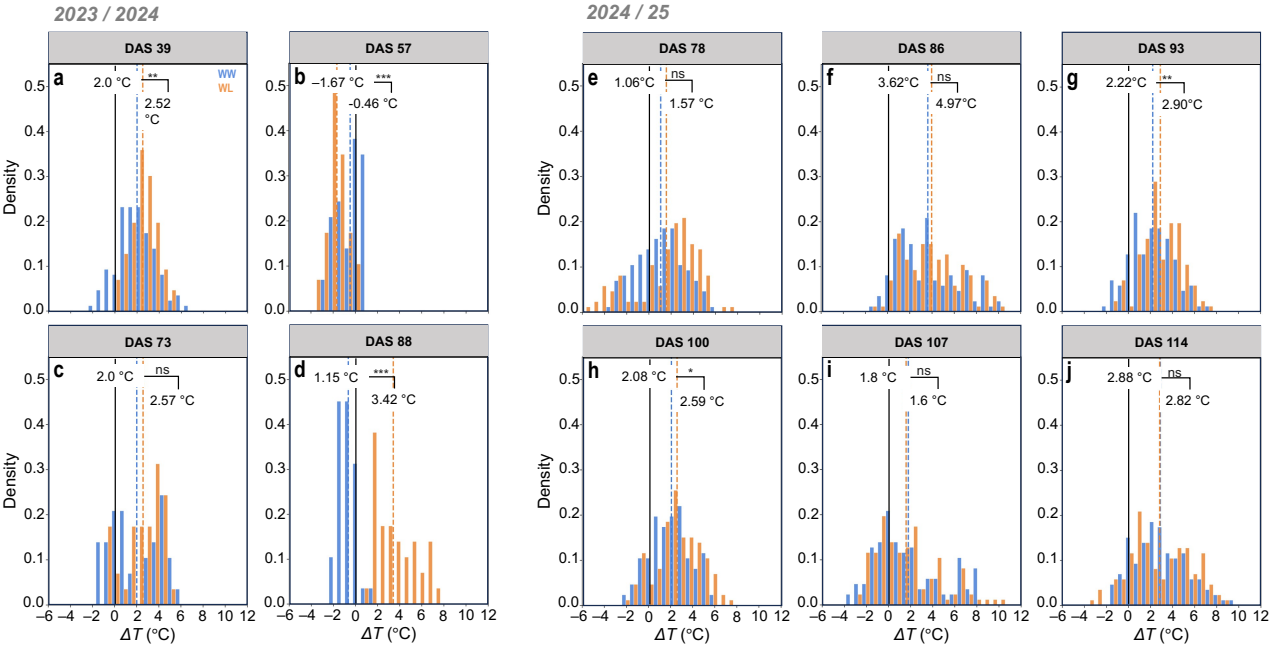

Figure S17. Same ad Figure S16 but for *ΔT*.

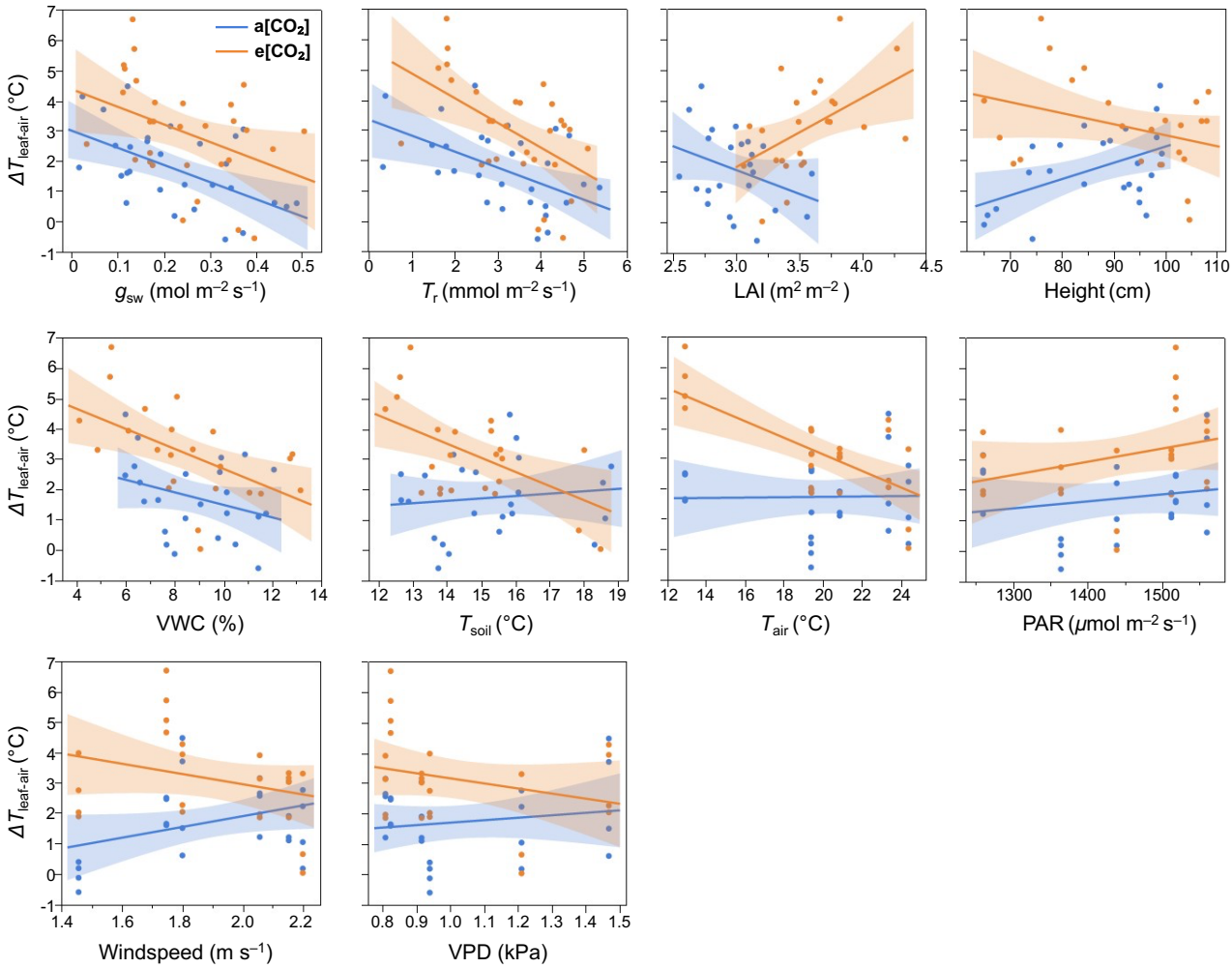

232

233 Figure S18. Scatter plots of plot-level ΔT and key physiological, structural, and environmental
234 variables under ambient (a[CO_2], blue) and elevated (e[CO_2], orange) [CO_2] conditions. Solid lines
235 show fitted linear trends with shaded 95% confidence intervals.

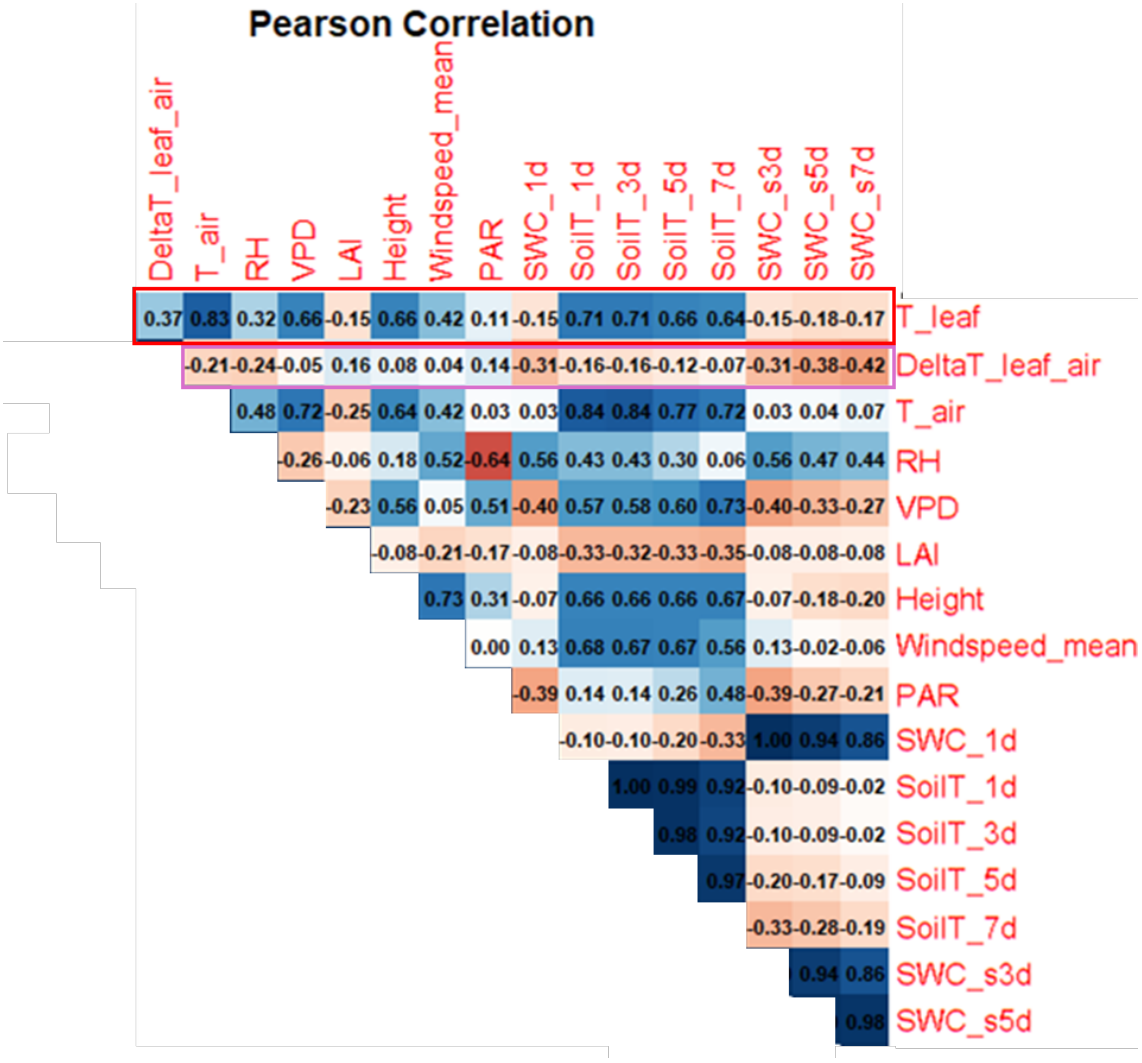

236

237 Figure S19. Pearson correlation matrix among ΔT and environmental and structural variables in the
238 2024/5 dataset (*Season 2*). Colors indicate the strength and sign of the correlation (positive – blue
239 and negative – red), and the values shown in each cell represent the correlation coefficient. Positive
240 values indicate that variables increase together, whereas negative values indicate an inverse
241 relationship. The matrix shows broadly consistent associations among variables, with strong
242 intercorrelations among soil temperature and soil water content metrics across temporal scales (1d
243 = same-day measurements; 3d, 5d, and 7d = mean values calculated over the respective periods of
244 3, 5, and 7 days preceding the day on which ΔT was measured). Red and purple outlines highlight
245 the matrix regions corresponding to pairwise relationships with ΔT variables.

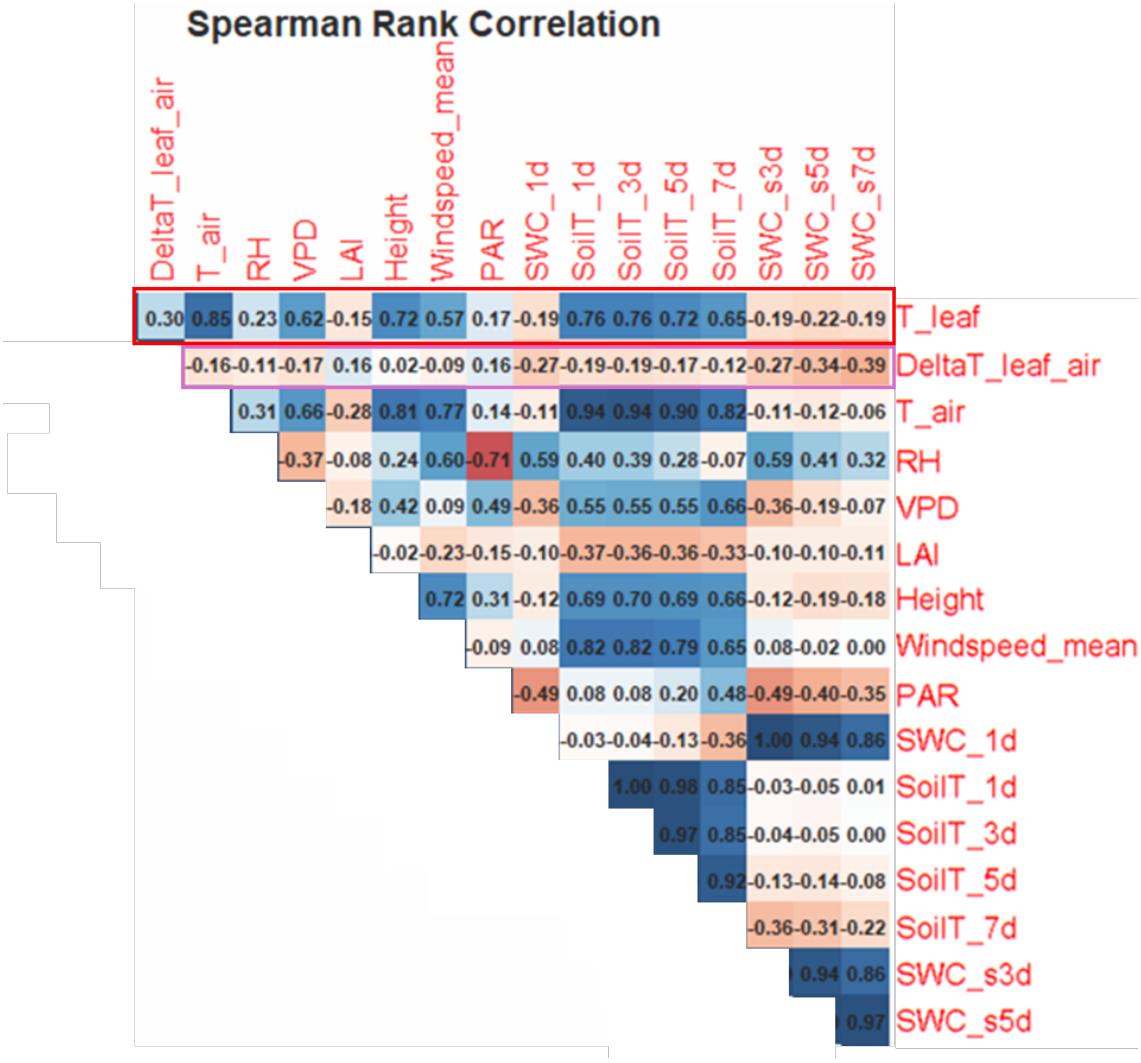

246

247 Figure S20. Same as in Figure S19, but for Spearman's rank correlation.

Supplementary Tables

Table S1. Meteorological conditions per season, including well-watered (WW) and limited-watered (WL) plots. R_g is global incoming radiation.

Season	*RH* (%)	T_{air} (°C)	*VPD* (kPa)	WW (mm)	WL (mm)	*ws* (m s^{-1})	R_g (W m^{-2} day^{-1})
2023/4	75 ± 16	15.2 ± 3.6	0.50 ± 0.43	464	323	1.21 ± 1.14	3200 ± 1082
2024/5	68 ± 12	15.5 ± 3.4	0.67 ± 0.41	403	372	1.11 ± 0.55	4246 ± 1605

Table S2. Corresponding Zadok decimal codes to days after sowing per genotype for cv. *Ruta* and cv. *Zahir*.

Season	DAS	Zadok decimal code (DC)	
		cv. *Ruta*	cv. *Zahir*
2023/4	39	DC23	DC32
	57	DC33	DC41
	73	DC41	DC55
	88	DC52	DC62
2024/5	78	DC37	DC55
	86	DC43	DC62
	93	DC52	DC65
	100	DC62	DC68
	107	DC65	DC77
	114	DC71	DC85

256 Table S3. The 41 sequential ΔT models.

Model	Variables included
B	Baseline
I	B + g_{sw} (mol m^{-2} s^{-1})
ii	B + *LAI* (m^2 m^{-2})
iii	B + height (cm)
iv	B + T_{soil} (˚C)
v	B + g_{sw} + [g_{sw} × *VPD*]
vi	B + g_{sw} + [g_{sw} × *VPD*] + *LAI*
vii	B + g_{sw} + [g_{sw} × *VPD*] + *LAI* + height
viii	B + g_{sw} + [g_{sw} × *VPD*] + *LAI* + height + T_{soil}
ix	B + g_{sw} + [g_{sw} × *VPD*] + [CO_2 × g_{sw}]
x	B + g_{sw} + [g_{sw} × *VPD*] + [CO_2 × g_{sw}] + *LAI*
xi	B + g_{sw} + [g_{sw} × *VPD*] + [CO_2 × g_{sw}] + *LAI* + height
xii	B + g_{sw} + [g_{sw} × *VPD*] + [CO_2 × g_{sw}] + *LAI* + height + T_{soil}
xiii	B + g_{sw} + [CO_2 × g_{sw}]
xiv	B + g_{sw} + [CO_2 × g_{sw}] + *LAI*
xv	B + g_{sw} + [CO_2 × g_{sw}] + *LAI* + height
xvi	B + g_{sw} + [CO_2 × g_{sw}] + *LAI* + height + T_{soil}
xvii	B + g_{sw} + [CO_2 × g_{sw}] + *LAI* + [CO_2 × *LAI*]
xviii	B + g_{sw} + [CO_2 × g_{sw}] + *LAI* + [CO_2 × *LAI*] + height
xix	B + g_{sw} + [CO_2 × g_{sw}] + *LAI* + [CO_2 × *LAI*] + height + [CO_2 × height]
xx	B + g_{sw} + [CO_2 × g_{sw}] + *LAI* + [CO_2 × *LAI*] + height + [CO_2 × height] + T_{soil}
xxi	B + g_{sw} + [CO_2 × g_{sw}] + *LAI* + [CO_2 × *LAI*] + height + [CO_2 × height] + T_{soil} + [*LAI* × T_{soil}]
xxii	B + g_{sw} + *LAI* + [CO_2 × *LAI*]
xxiii	B + g_{sw} + *LAI* + [CO_2 × *LAI*] + height
xxiv	B + g_{sw} + *LAI* + [CO_2 × *LAI*] + height + T_{soil}
xxv	B + g_{sw} + *LAI* + [CO_2 × *LAI*] + height + T_{soil} + [*LAI* × T_{soil}]
xxvi	B + g_{sw} + [g_{sw} × *VPD*] + *LAI* + [CO_2 × *LAI*]
xxvii	B + g_{sw} + [g_{sw} × VPD] + *LAI* + [CO_2 × *LAI*] + height
xxviii	B + g_{sw} + [g_{sw} × VPD] + *LAI* + [CO_2 × *LAI*] + height + T_{soil}
xxix	B + g_{sw} + [g_{sw} × VPD] + *LAI* + [CO_2 × *LAI*] + height + T_{soil} + [*LAI* × T_{soil}]
xxx	B + g_{sw} + *LAI* + height + [CO_2 × *LAI*] + [CO_2 × height]
xxxi	B + g_{sw} + *LAI* + height + [CO_2 × *LAI*] + [CO_2 × height] + T_{soil}
xxxii	B + g_{sw} + *LAI* + height + [CO_2 × *LAI*] + [CO_2 × height] + T_{soil} + [*LAI* × T_{soil}]
xxxiii	B + g_{sw} + [g_{sw} × *VPD*] + *LAI* + [CO_2 × *LAI*] + height + [CO_2 × height]
xxxiv	B + g_{sw} + [g_{sw} × *VPD*] + *LAI* + [CO_2 × *LAI*] + height + [CO_2 × height] + T_{soil}
xxxv	B + g_{sw} + [g_{sw} × *VPD*] + *LAI* + [CO_2 × *LAI*] + height + [CO_2 × height] + T_{soil} + [*LAI* × T_{soil}]
xxxvi	B + g_{sw} + [CO_2 × g_{sw}] + [g_{sw} × *VPD*] + *LAI* + [CO_2 × *LAI*]
xxxvii	B + g_{sw} + [CO_2 × g_{sw}] + [g_{sw} × *VPD*] + *LAI* + [CO_2 × *LAI*] + height
xxxviii	B + g_{sw} + [CO_2 × g_{sw}] + [g_{sw} × *VPD*] + *LAI* + [CO_2 × *LAI*] + height + T_{soil}
xxxix	B + g_{sw} + [CO_2 × g_{sw}] + [g_{sw} × *VPD*] + *LAI* + [CO_2 × *LAI*] + height + T_{soil} + [*LAI*× T_{soil}]
xxxx	B + g_{sw} + [CO_2 × g_{sw}] + [g_{sw} × *VPD*] + *LAI* + [CO_2 × *LAI*] + height + [CO_2 × height] + T_{soil} + [*LAI* × T_{soil}]

Table S4. Statistics of the 41-step sequential ΔT modelling. Directional (β) and nonlinear (γ) coefficients represent the linear and quadratic terms, respectively, within the modelling framework. In red are the statistically significant coefficients ($p < 0.05$), while bold italics denote marginal significance ($0.05 \leq p < 0.10$). B is the baseline model and models *i–xxxx* correspond to the models presented in Table S3.

Model	β_{CO2}	AICc	R^2	R^2adj	RMSE	β_{gsw}	β_{LAI}	β_{height}	β_{Tsoil}	γ_{gsw}	γ_{LAI}	γ_{height}	γ_{Tsoil}
B	0.52	374.7	0.38	0.31	1.77								
i	0.52	323.3	0.47	0.40	1.60	-0.43				0.10			
ii	0.54	326.3	0.48	0.40	1.58	-0.40	0.01			0.09	0.09		
iii	0.58	326.0	0.50	0.42	1.55	-0.36	0	0.22		0.05	0.07	-0.29	
iv	0.49	327.7	0.52	0.43	1.52	-0.35	0.01	0.29	-0.04	0.06	0.07	***-0.25***	***0.27***
v	0.52	325.9	0.47	0.39	1.60	-0.42				0.10			
vi	0.54	329.0	0.48	0.40	1.58	-0.39	0.01			0.08	0.09		
vii	0.58	328.9	0.50	0.41	1.55	-0.35	-0.01	0.22		0.05	0.07	-0.29	
viii	0.49	330.7	0.52	0.42	1.52	-0.35	0.01	0.30	-0.04	0.06	0.07	***-0.25***	***0.27***
ix	0.53	327.0	0.48	0.40	1.59	-0.35				0.10			
x	0.57	329.9	0.49	0.40	1.57	-0.31	-0.01			0.08	0.09		
xi	0.64	328.8	0.51	0.42	1.53	***-0.24***	-0.02	0.16		0.05	0.07	-0.31	
xii	0.56	331.3	0.53	0.43	1.51	***-0.25***	0	0.24	-0.03	0.06	0.07	-0.27	0.25
xiii	0.53	324.4	0.47	0.40	1.59	-0.37				0.10			
xiv	0.57	327.2	0.49	0.40	1.57	-0.32	-0.01			0.09	0.09		
xv	0.64	326.0	0.51	0.42	1.53	***-0.26***	-0.02	0.17		0.05	0.07	-0.31	
xvi	0.56	328.2	0.53	0.43	1.51	***-0.25***	0	0.24	-0.02	0.06	0.07	-0.27	***0.26***
xvii	0.55	327.6	0.50	0.41	1.56	-0.32	-0.17			0.10	0.01		
xviii	0.59	326.3	0.52	0.43	1.52	-0.26	-0.20	0.25		0.07	-0.01	-0.31	
xix	0.62	323.6	0.54	0.45	1.48	-0.32	-0.16	0.39		0.06	0.02	-0.14	
xx	0.56	328.0	0.55	0.45	1.47	-0.31	-0.13	0.42	-0.01	0.06	0.03	-0.13	0.18
xxi	0.56	331.2	0.55	0.44	1.47	-0.31	-0.11	0.42	0.02	0.06	0.04	-0.14	0.20
xxii	0.52	327.1	0.49	0.40	1.57	-0.41	-0.13			0.10	0.02		
xxiii	0.53	326.7	0.51	0.42	1.54	-0.37	-0.17	0.30		0.06	0	-0.29	
xxiv	0.47	329.2	0.52	0.43	1.52	-0.35	-0.12	0.36	0	0.07	0.01	***-0.25***	0.25
xxv	0.47	331.9	0.52	0.42	1.51	-0.34	-0.18	0.36	-0.08	0.06	-0.01	-0.21	0.20
xxvi	0.52	330.0	0.49	0.40	1.57	-0.40	-0.13			0.09	0.02		
xxvii	0.53	329.7	0.51	0.42	1.54	-0.36	-0.17	0.30		0.06	0	-0.29	
xxviii	0.47	332.3	0.52	0.42	1.52	-0.36	-0.13	0.36	0.01	0.07	0.01	***-0.24***	0.25
xxix	0.47	335.1	0.52	0.42	1.51	-0.34	-0.18	0.36	-0.07	0.06	-0.01	-0.21	0.20
xxx	0.57	323.2	0.53	0.44	1.5	-0.42	-0.13	0.44		0.05	0.03	-0.11	
xxxi	0.51	327.2	0.54	0.44	1.49	-0.40	-0.10	0.47	-0.04	0.06	0.04	-0.10	0.19
xxxii	0.51	330.3	0.54	0.44	1.49	-0.41	-0.09	0.47	-0.02	0.06	0.04	-0.10	0.20
xxxiii	0.57	326.1	0.53	0.44	1.5	-0.41	-0.13	0.44		0.05	0.03	-0.11	
xxxiv	0.51	330.3	0.54	0.44	1.49	-0.40	-0.10	0.47	-0.04	0.06	0.04	-0.10	0.19
xxxv	0.51	333.6	0.54	0.43	1.49	-0.40	-0.09	0.47	-0.02	0.06	0.04	-0.10	0.20
xxxvi	0.55	330.4	0.50	0.41	1.56	-0.30	-0.17			0.10	0.01		
xxxvii	0.60	329.2	0.52	0.43	1.52	***-0.24***	-0.20	0.25		0.06	-0.01	-0.31	
xxxviii	0.53	332.5	0.53	0.43	1.50	***-0.25***	-0.15	0.31	0.03	0.07	0	-0.27	0.23
xxxix	0.53	335.5	0.53	0.42	1.50	***-0.24***	-0.2	0.31	-0.04	0.06	-0.02	-0.24	0.19
xxxx	0.57	334.4	0.55	0.44	1.47	-0.31	-0.11	0.42	0.01	0.06	0.04	-0.14	0.19

Notes: All R^2 are significant at $p < 0.0001$; RMSE is in °C. Nonlinear coefficients were estimated for the quadratic term within the hierarchical mixed model.

Table S5. Statistics of the main ΔT models used in the main manuscript. Directional (β) and nonlinear (γ) coefficients represent the linear and quadratic terms, respectively, within the modelling framework. In red are the statistically significant coefficients ($p < 0.05$), while bold italics denote marginal significance ($0.05 \leq p < 0.10$). B is the baseline model, and $+g_{sw}$, $+LAI$, +height, and $+T_{soil}$ models correspond to *v*, *xxvi*, *xxvii*, and *xxix* in Table S4.

Model	β_{CO2}	AICc	R^2	R^2adj	RMSE	β_{gsw}	β_{LAI}	β_{height}	β_{Tsoil}	γ_{gsw}	γ_{LAI}	γ_{height}	γ_{Tsoil}
B	0.52	374.7	0.38	0.31	1.77								
+ g_{sw}	0.52	325.9	0.47	0.39	1.60	-0.42				0.10			
+ *LAI*	0.52	330.0	0.49	0.40	1.57	-0.40	-0.13			0.09	0.02		
+ height	0.53	329.7	0.51	0.42	1.54	-0.36	-0.17	0.30		0.06	0	-0.29	
+ T_{soil}	0.47	335.1	0.52	0.42	1.51	-0.34	-0.18	0.36	-0.07	0.06	-0.01	-0.21	0.20

Table S6. Statistics of the ΔT models excluding [CO_2] from the model. Directional (β) and nonlinear (γ) coefficients represent the linear and quadratic terms, respectively, within the modelling framework. In red are the statistically significant coefficients ($p < 0.05$), while bold italics denote marginal significance ($0.05 \leq p < 0.10$).

Model	AICc	R^2	R^2adj	RMSE	β_{gsw}	β_{LAI}	β_{height}	β_{Tsoil}	γ_{gsw}	γ_{LAI}	γ_{height}	γ_{Tsoil}
B	386.2	0.31	0.25	0.83								
+ g_{sw}	335.4	0.41	0.33	0.76	-0.39				0.04			
+ [g_{sw} × *VPD*]	338.0	0.41	0.33	0.76	-0.38				0.04			
+ *LAI*	337.7	0.43	0.35	0.74	-0.45	0.19			0.08	0.08		
+ height	337.7	0.46	0.36	0.72	-0.42	0.11	***0.49***		0.05	0.09	***-0.24***	
B + g_{sw} + *LAI*	335.0	0.43	0.35	0.74	-0.46	0.19			0.08	0.08		
+ height	334.8	0.46	0.37	0.72	-0.43	0.11	***0.49***		0.05	0.09	***-0.24***	
+ T_{soil}	332.5	0.49	0.40	0.70	-0.41	0.10	***0.50***	-0.35	0.08	0.09	-0.22	0.31
+ [g_{sw} × *VPD*]	335.5	0.49	0.39	0.70	-0.42	0.10	***0.50***	-0.34	0.08	0.09	-0.22	***0.32***
+ [*LAI* × T_{soil}]	338.5	0.49	0.38	0.70	-0.42	0.09	***0.50***	-0.36	0.07	0.09	-0.21	***0.30***

References

1. Israel Meteorological Service.
2. Miglietta, F. *et al.* Free-air CO2 enrichment (FACE) of a poplar plantation: the POPFACE fumigation system. *New Phytol.* **150**, 465–476 (2001).
3. Mollah, M., Norton, R. & Huzzey, J. Australian grains free-air carbon dioxide enrichment (AGFACE) facility: Design and performance. *Crop Pasture Sci.* **60**, 697–707 (2009).
4. Reis, M. G. dos & Ribeiro, A. Conversion factors and general equations applied in agricultural and forest meteorology. *Agrometeoros* **27**, 227–258 (2020).
5. Helman, D., Lensky, I. M. & Bonfil, D. J. Early prediction of wheat grain yield production from root-zone soil water content at heading using Crop RS-Met. *F. Crop. Res.* **232**, (2019).
6. Bonfil, D. J., Richkar, I. & Gilboa, A. Wheat cultivars in Israel: a multiyear summary 2007-2017 (Hebrew). *Nir Vatelem* 6–10 (2018).